



# Iceberg size and orientation estimation using SeaWinds

K.M. Stuart, D.G. Long\*

Microwave Earth Remote Sensing Laboratory, Brigham Young University, 459 CB, Provo, UT 84602, United States

## ARTICLE INFO

### Article history:

Received 11 February 2011  
Accepted 16 July 2011

### Keywords:

SeaWinds  
Scatterometer  
Icebergs  
Estimation  
Maximum-likelihood estimation

## ABSTRACT

SeaWinds scatterometer data from 1999 to 2009 has been used to detect and track large Antarctic icebergs on a daily basis. Here, we develop two estimation algorithms to supplement iceberg position reports with estimates of the iceberg's major-axis length, minor-axis length, and angle of rotational orientation. The first algorithm is an image-based approach while the second is based on raw SeaWinds measurements. Maximum-likelihood objective functions that relate SeaWinds backscatter observations to model predictions are developed. The utility of both estimation approaches is analyzed in simulation and with actual data via a case study of iceberg A22a. The image-based approach is found to outperform the measurement-based technique. Results are validated using high-resolution imagery. Estimates are also compared with reports compiled by the United States National Ice Center.

© 2011 Elsevier B.V. All rights reserved.

## 1. Introduction

Knowledge of iceberg locations is important for safety reasons as well as for understanding many geophysical and biological processes. For instance, iceberg positions affect shipping lanes, outline ocean currents, and influence biological productivity. Observed physical and electromagnetic characteristics of icebergs are also useful in estimating local weather conditions. Furthermore, the impact of an iceberg on its environment is related to iceberg properties such as physical size and spatial orientation. Because of the importance of modeling the effects of icebergs in these regards, frequent iceberg observations are needed.

The United States National Ice Center (NIC) plays a major role in tracking the location of Antarctic icebergs. Current NIC methods for tracking icebergs primarily involve using optical satellite imagery, augmented by synthetic aperture radar (SAR) and scatterometer images. Optical sensors produce high-resolution images but are unable to penetrate cloud cover and are dependent on solar illumination. Despite the high-resolution inherent in optical and SAR images, the spatial coverage of these sensors is limited, frequently resulting in poor temporal resolution. As a result, the NIC has updated iceberg positions around every 20 days in the last decade. NIC updates detail iceberg location and size.

To supplement iceberg reports from the NIC, the utility of the SeaWinds scatterometer to track large tabular icebergs on a daily basis in the Southern Ocean has also been documented. Even though SeaWinds was never designed to track icebergs, an extensive Antarctic iceberg database detailing positions of large tabular icebergs has been derived from SeaWinds data and is used in this study. Using reconstruction-enhanced scatterometer images, icebergs are manually tracked on a daily basis and are cataloged as part of the Scatterometer

Record Pathfinder Project at Brigham Young University's Microwave Earth Remote Sensing (MERS) Laboratory. These floating glacial ice fragments are generally larger than 5 km and are typically characterized as a rough ice plateau above the water (Long and Ballantyne, 2002; SCP, update, 2010; Stuart and Long, 2011).

This paper extends the analysis of SeaWinds iceberg observations to include iceberg major-axis length, minor-axis length, and rotational orientation via automated maximum-likelihood (ML) estimation techniques. This paper presents an iceberg model to characterize iceberg dimensions and develops both an image-based and a measurement-based approach to estimate the parameters of the iceberg model from SeaWinds backscatter data. Objective functions for each case are developed. Simulation is employed to explore and compare the effectiveness of each algorithm. Finally, the algorithms are explored via a case study of iceberg A22a. Subsequent image-based and measurement-based estimates are compared with estimates extracted from high-resolution imagery and reports collected by the United States National Ice Center (NIC).

This paper is organized as the following: Section 2 reviews pertinent information about the SeaWinds instrument and corresponding high-resolution image products used to track icebergs. Section 3 presents the model used to characterize size and shape of icebergs. Section 4 outlines the objective functions for both the image-based and measurement-based estimates. Section 5 describes the implementation for both algorithms in both a simulation and in a case study. Section 6 concludes.

## 2. Background

### 2.1. SeaWinds

SeaWinds is a Ku-band scanning pencil-beam scatterometer aboard the QuikSCAT spacecraft and is designed to determine the normalized radar cross section,  $\sigma^0$ , of the Earth's surface. Its sun-synchronous polar

\* Corresponding author.

E-mail addresses: [stuart@mers.byu.edu](mailto:stuart@mers.byu.edu) (K.M. Stuart), [long@ee.byu.edu](mailto:long@ee.byu.edu) (D.G. Long).

orbit allows for complete daily coverage of the polar regions. SeaWinds has two scanning conical beams. The outer beam is vertically polarized at a nominal incidence angle of 54°; the inner beam is horizontally polarized at a nominal incidence angle of 46°. This design provides for four independent observations of the region lying within the inner swath and two independent observations of targets contained within the outer swath (Early and Long, 2001; Spencer and Long, 2000). Because SeaWinds operates at microwave frequencies, its radar measurements penetrate cloud cover and are independent of solar illumination.

Using onboard range-Doppler processors, SeaWinds backscatter values for each microwave pulse are separated into spatial regions called slices where each has a separate  $\sigma^\circ$  value (Dunbar et al., 2006). Because of the rapid roll-off of the aperture response function corresponding to each slice, individual response patterns are frequently represented as a binary mask corresponding to the 6 dB contour of each slice footprint, measuring approximately  $6 \times 25$  km (Ashcraft and Long, 2003).

Slice backscatter measurements can be modeled as a combination of the true signal power  $\sigma_t^\circ$  and multiplicative noise, specifically (Dunbar et al., 2006)

$$\sigma^\circ = \sigma_t^\circ (1 + K_p \nu) \quad (1)$$

where  $\sigma_t^\circ$  is the true backscatter,  $K_p$  is a dimensionless coefficient embodying all geophysical and instrumentation noise, and  $\nu$  is a Gaussian random variable with zero mean and unit variance. Because each range-Doppler-filtered slice has a large spatial footprint compared to the operating wavelength, each  $\sigma_t^\circ$  may be modeled as a linear combination of spatial backscatter distributions,

$$\sigma_t^\circ = \frac{\int R(\tau) \sigma_{pt}^\circ(\tau) d\tau}{\int R(\tau) d\tau} \quad (2)$$

where  $R(\tau)$  is the spatial response function of the two-dimensional ground illumination footprint and  $\sigma_{pt}^\circ(\tau)$  is the spatial distribution of  $\sigma_t^\circ$  at the Earth's surface. The integrals are over the antenna footprint with respect to the two-dimensional spatial index  $\tau$  (Spencer et al., 1997). Note that in many applications, as well as in this study,  $R(\tau)$  is simplified and represented as a binary mask that corresponds to the 6 dB antenna footprint (Ashcraft and Long, 2003; Williams et al., 2009).

Eq. (1) can be written as

$$\sigma^\circ = \sigma_t^\circ + \nu' \quad (3)$$

where  $\nu' \sim N(0, K_p^2 \sigma_t^{\circ 2})$ . For SeaWinds  $K_p = \sqrt{\alpha + \beta / \sigma_t^\circ + \gamma / \sigma_t^{\circ 2}}$  where  $\alpha$ ,  $\beta$ , and  $\gamma$  are related to the signal-to-noise ratio and the parameters of the radar equation. These values are computed for each spatial response function (Dunbar et al., 2006). The corresponding probability distribution function of a single  $\sigma^\circ$  measurement can explicitly be modeled as

$$P(\sigma^\circ | \sigma_t^\circ) = \frac{1}{\sqrt{2\pi\xi}} \exp\left\{-\frac{(\sigma^\circ - \sigma_t^\circ)^2}{2\xi^2}\right\} \quad (4)$$

where  $\xi^2 = \alpha \sigma_t^{\circ 2} + \beta \sigma_t^\circ + \gamma$ .

## 2.2. Resolution enhancement

While individual  $\sigma^\circ$  measurements are useful in point-target analysis, it is desirable to generate backscatter images for macro-scale studies. The dense sampling of SeaWinds measurements in the polar regions facilitates use of image reconstruction techniques to produce higher-resolution images (Spencer and Long, 2000). The scatterometer

image reconstruction (SIR) algorithm combines multiple backscatter measurements into a composite image with higher-spatial resolution than the associated aperture response via reconstruction techniques. SIR is an iterative multiplicative algebraic reconstruction technique that combines overlapping measurements to produce a resolution-enhanced backscatter image (Early and Long, 2001).

The SIR algorithm depends on dense, overlapping measurements which are assured by using radar measurements from multiple satellite passes. This results in a trade-off between spatial and temporal resolution. Images reconstructed from slice measurements have an effective resolution of 4–5 km and are reported on a 2.225 km grid (Early and Long, 2001). SIR images are produced as standard SeaWinds image data products at BYU and distributed world-wide (SCP, update, 2010).

## 2.3. Preliminary iceberg estimate methodology

Previously, various studies have been performed using SeaWinds SIR images to estimate iceberg parameters. One approach estimates iceberg position using a subjective, manual process along with previous location information to track daily iceberg position in SIR images (Stuart and Long, 2011). Because it requires human input, this methodology is time-intensive and contains errors related to the competency level and experience of the analyst. In a second historical approach, iceberg position is extracted from daily SIR imagery using known iceberg statistics via a correlation method (Stephen and Long, 2000). Previously, information regarding iceberg size has primarily only been obtainable from high-resolution optical imagery which has limited spatial and temporal coverage, suffers from cloud interference, and depends on external illumination. In this paper we are interested in the inverse of the problem presented in Stephen and Long (2000), i.e. we estimate fundamental iceberg characteristics such as position, shape, and size given estimates of the previous position.

A particular methodology is based on using daily SeaWinds SIR images. Consider a backscatter image that contains an iceberg such that only the iceberg and the immediately-surrounding background is visible. We are interested in classifying each pixel in the image as either corresponding to an iceberg or a non-iceberg medium. Backscatter images of the Southern Ocean primarily consist of open water, sea ice, and glacial ice. If the backscatter values corresponding to the iceberg and the background are relatively homogeneous, then a classification scheme such as a simple Neyman–Pearson hypothesis test can be used to classify each resolution cell. The resulting binary image can then be analyzed to determine overall iceberg shape and size. Troglia et al. (2010), in mapping craters in an image, fit a model to a binary image. The estimates of the model were the estimates of the crater size. The same approach can be used for icebergs. While this thresholding approach is numerically efficient, its effectiveness varies with the noise level in backscatter images. Furthermore it is limited to homogeneous scenes and does not work well when the iceberg is near the sea-ice edge. Consequently, a more robust estimation methodology is needed to estimate iceberg size and shape using SeaWinds SIR images.

We propose using an elliptical model to describe the size and shape of an iceberg because it has a simple construction with few parameters and, to first order, it conforms to the general shape of large tabular icebergs (Bigg et al., 1997; Crocker, 1993; Savage et al., 2000). Furthermore we propose using SeaWinds data to estimate the parameters of this model, specifically major-axis length, minor-axis length, and angle of orientation. There are two potential levels of SeaWinds data that can be used in the estimation process, the previously-mentioned SIR backscatter images and the raw SeaWinds measurements. Consequently, two model-based estimation approaches are proposed: one based on images and the other based on the raw data. The elliptical model used to describe iceberg size and shape is developed

in Section 3. The approaches used to estimate model parameters are derived in Section 4.

### 3. Iceberg model

This section develops the model used to characterize the top-down shape of large tabular icebergs. As previously mentioned, a generalized elliptical model is chosen because it is a simple construction with few parameters and, to first order, it reflects the general top-down shape of large tabular icebergs (Bigg et al., 1997; Crocker, 1993; Savage et al., 2000). The iceberg backscatter is modeled as nearly constant over an elliptical shape with the edges of the shape smoothed via a simple spatial window. This results in an elliptically-shaped bump with slightly rounded edges. Formally, a simple analytic form for spatially modeling the backscatter profile of a large tabular iceberg is

$$\sigma^\circ(x, y, \bar{\alpha}) = (A-B) \cdot \exp\left\{-\left(|a|^p + |b|^p\right)^{\frac{1}{p}}\right\} + B \quad (5)$$

where

$$a = \frac{(x-\mu_x) \cos(\theta) + (y-\mu_y) \sin(\theta)}{\rho_{ma}}$$

and

$$b = \frac{(x-\mu_x) \sin(\theta) - (y-\mu_y) \cos(\theta)}{\rho_{mi}}$$

where  $x$  and  $y$  are the free-space indices of the 2-dimensional grid on the Earth's surface. In Eq. (5), the variable  $A$  defines the center backscatter value corresponding to glacial ice, and  $B$  is the background backscatter value. The parameter  $n$  controls the sharpness of the transition between  $A$  and  $B$  where a larger  $n$  results in a smaller transition band. Variables  $\mu_x$  and  $\mu_y$  define the center with respect to the local frame. Parameters  $\rho_{ma}$  and  $\rho_{mi}$  correspond to the length of the major and minor axes, respectively. The variable  $\theta$  is the angle of orientation of the major axis with respect to the local frame where  $0^\circ$  corresponds to horizontal position and a positive increasing angle corresponds to clockwise motion. The super-ellipse parameter  $p$  controls the squareness of the ellipse. Note that functionally,  $p$  is only required to be positive, however for purposes of shape estimation, there is a potential shape ambiguity between models when  $p$  is unity and when  $p$  is large. Therefore, to prevent geometric ambiguity,  $p$  is limited to the range  $p \in [1, 2]$ . The model parameters in Eq. (5) constitute  $\bar{\alpha}$ , the model parameter vector where  $\bar{\alpha} = [A, B, n, p, \mu_x, \mu_y, \rho_{ma}, \rho_{mi}, \theta]$ .

Example instances of Eq. (5) are displayed in Fig. 1 for  $A = 1$ ,  $B = 0$ , variable  $n$  and  $p$ , arbitrary  $\mu_x$  and  $\mu_y$ ,  $\rho_{ma} = 2\rho_{mi}$ , and  $\theta = 45^\circ$ . We note that increasing  $n$  results in a more plateau-like model and decreasing  $p$  results in the elliptical model becoming more squared.

We find that icebergs of adequate size and sufficient backscatter contrast result in accurate model parameter estimates. However, if the size or contrast is insufficient, the solution space becomes ill-conditioned, potentially resulting in degenerate estimates. For instance, if an iceberg is rounded in shape, the major-axis length and minor-axis length are similar in value and the angle estimate may be ill-conditioned. Also, if an iceberg's size reduces to the order of the size of the ground illumination footprint, image contrast decreases. The backscatter contrast necessary for successful parameter estimation is discussed in Section 5.1. Degenerate estimation cases are discussed more in Section 5.4.

### 4. Estimation algorithm

To estimate the position, shape, and rotational orientation of tabular icebergs using the model, two estimation methodologies are presented in this section. In the first, iceberg model parameters are derived from

SeaWinds SIR images. In the second, the parameters are estimated directly from raw SeaWinds measurements without forming an image. These two approaches are referred to as the image-based (IB) and measurement-based (MB) estimation approaches, respectively. Both approaches have advantages and limitations. First, image-based estimation is explored. Next, measurement-based estimation is developed, then the two algorithms are compared. Last, assumptions and implications inherent from using the iceberg model in the estimation process are discussed.

#### 4.1. Image-based estimation

To estimate iceberg size and rotational orientation from the SeaWinds backscatter images, we use the standard enhanced-resolution SeaWinds h-pol SIR backscatter images as input. Because a SIR image consists of a combination of measurements, each pixel backscatter value  $\sigma_{pix}^\circ$  is a function of the raw measurements described in Eq. (3). The backscatter at each pixel may be expressed as a combination of a true pixel-wise signal power and additive noise, i.e.  $\sigma_{pix}^\circ = \sigma_{pix,t}^\circ + \nu$  where  $\nu$  is the effective noise. Although iceberg parameters are estimated over a temporal window of 24 h,  $\sigma_{pix,t}^\circ$  is considered a constant in the estimation process. The corresponding probability distribution function of  $\sigma_{pix}^\circ$  can be modeled as

$$P(\sigma_{pix}^\circ | \sigma_{pix,t}^\circ) = \frac{1}{\sqrt{2\pi}\xi_{pix}} \exp\left\{-\frac{(\sigma_{pix}^\circ - \sigma_{pix,t}^\circ)^2}{2\xi_{pix}^2}\right\} \quad (6)$$

where  $\xi_{pix}^2$  is the variance of  $\sigma_{pix}^\circ$  and is computed in the SIR reconstruction process (Spencer and Long, 2000). We estimate  $\sigma_{pix,t}^\circ$  using the iceberg model developed in Eq. (5) to select the model parameters  $\bar{\alpha}$  that maximize the probability of  $\sigma_{pix}^\circ$  given  $\sigma_c^\circ(x, y, \bar{\alpha})$ .

The estimation process minimizes the difference between the measured backscatter and the model-based construction by adjusting model parameters. For a single pixel  $(x_0, y_0)$ , this probability distribution is

$$P(\sigma_{pix}^\circ(x_0, y_0) | \sigma_c^\circ(x_0, y_0, \bar{\alpha})) = \frac{1}{\sqrt{2\pi}\xi_{pix}(x_0, y_0)} \exp\left\{-\frac{[\sigma_{pix}^\circ(x_0, y_0) - \sigma_c^\circ(x_0, y_0, \bar{\alpha})]^2}{2\xi_{pix}^2(x_0, y_0)}\right\} \quad (7)$$

For multiple pixels and assuming each pixel is mutually independent of adjacent pixels, the joint distribution of  $\sigma_{pix}^\circ(x, y)$  given  $\sigma_c^\circ(x, y, \bar{\alpha})$  is a joint distribution of independent Gaussian random variables and has the form

$$P(\bar{\sigma}_{pix}^\circ(x, y) | \bar{\sigma}_c^\circ(x, y, \bar{\alpha})) = \prod_{x,y \in X,Y} P(\sigma_{pix}^\circ(x, y) | \sigma_c^\circ(x, y, \bar{\alpha})) \quad (8)$$

where  $\bar{\sigma}_{pix}^\circ(x, y)$  and  $\bar{\sigma}_c^\circ(x, y, \bar{\alpha})$  represent vectorized forms of  $\sigma_{pix}^\circ(x, y)$  and  $\sigma_c^\circ(x, y, \bar{\alpha})$  and where  $(X, Y)$  spans the image of estimation.

Maximizing Eq. (8) yields a maximum-likelihood estimate. However, for practical purposes, we maximize the log of Eq. (8). The image-based ML estimate of  $\bar{\alpha}$  may be expressed as

$$\bar{\alpha}_{IB}^* = \underset{\bar{\alpha}}{\operatorname{argmax}} \left\{ \log P(\bar{\sigma}_{pix}^\circ(x, y) | \bar{\sigma}_c^\circ(x, y, \bar{\alpha})) \right\} \quad (9)$$

where  $\bar{\alpha}_{IB}^*$  is the parameter vector that maximizes Eq. (8). Explicitly solving Eq. (9) and simplifying by removing constant terms yields

$$\bar{\alpha}_{IB}^* = \underset{\bar{\alpha}}{\operatorname{argmin}} \sum_{x,y \in X,Y} \left[ \frac{[\sigma_{pix}^\circ(x, y) - \sigma_c^\circ(x, y, \bar{\alpha})]^2}{\xi_{pix}^2(x, y)} + \ln(\xi_{pix}^2(x, y)) \right] \quad (10)$$

However, low variances in our data cause the left term in brackets in Eq. (10) to occasionally become ill-conditioned. As a result, a

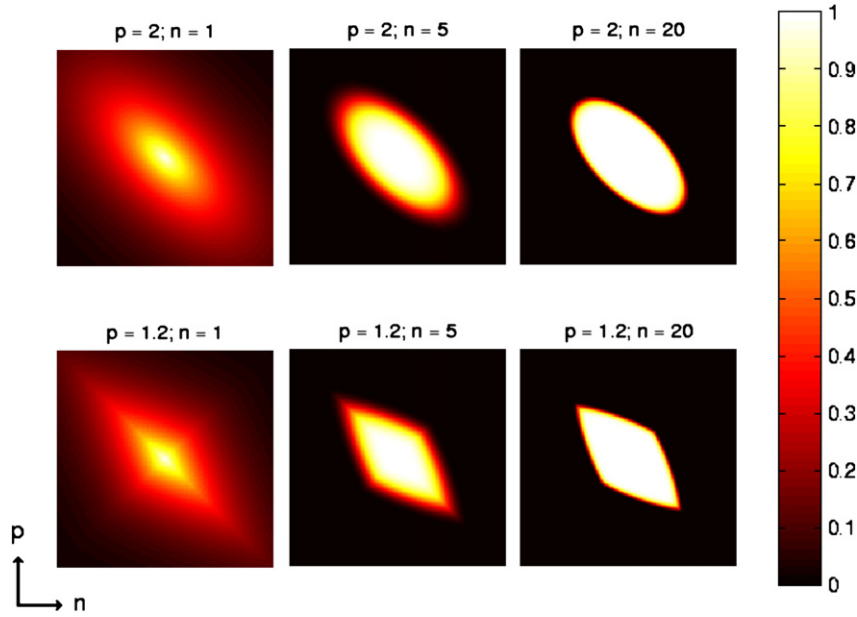


**Fig. 1.** Iceberg model (Eq. 5) plotted for various realizations of  $\bar{\alpha} = [1, 0, n, p, \mu_x, \mu_y, 2\rho_{mi}, \rho_{mi}, 45^\circ]$  where  $n$  and  $p$  are varied with  $\mu_x$  and  $\mu_y$  chosen to correspond to the center of the region. The horizontal scale is arbitrary.

variance-regularization term,  $\lambda_{IB}$ , is introduced so that Eq. (10) becomes

$$\bar{\alpha}_{IB}^* = \underset{\bar{\alpha}}{\operatorname{argmin}} \sum_{x,y \in X,Y} \left[ \frac{(\sigma_{pix}^o(x,y) - \sigma_c^o(x,y,\bar{\alpha}))^2}{\chi_{pix}^2(x,y)} + \ln(\chi_{pix}^2(x,y)) \right] \quad (11)$$

where  $\chi_{pix}^2(x,y) = (1 - \lambda_{IB}) + \lambda_{IB} \cdot \xi_{pix}^2(x,y)$  where  $\lambda_{IB} \in [0, 1]$ . The  $\lambda_{IB} = 0$  case corresponds to a least-squares objective function while  $\lambda_{IB} = 1$  corresponds to the image-based maximum-likelihood case. We can vary  $\lambda_{IB}$  to allow us to select an estimation approach that lies between these two cases which can be useful to mitigate the adverse effects of low image contrast or image contamination. This is discussed further in Section 5.4.

Choosing  $\bar{\alpha}$  to maximize the objective function provides the best fit in a maximum-likelihood sense for the parameters of the model, thereby yielding estimates of the size and orientation of the iceberg. By repeating this to produce a time-series of estimates, we obtain the evolution of the size and rotation of the iceberg.

#### 4.2. Measurement-based estimation

The measurement-based estimation approach uses the individual slice measurements and their associated spatial response functions directly without first forming an image. The measurement-based approach can be derived similarly to the image-based case (Eq. 6–11) if the pixel backscatter,  $\sigma_{pix}^o(x,y)$ , is replaced with the SeaWinds backscatter measurements,  $\sigma^o(j)$ , where  $j$  indexes the set of raw SeaWinds measurements; the modeled backscatter,  $\sigma_c^o(x,y,\bar{\alpha})$ , is replaced with a measurement-referenced model backscatter term,  $\sigma_c^o(j,\bar{\alpha})$ ; and the pixel-based variance,  $\xi_{pix}^2(x,y)$ , is replaced with  $\xi^2(j)$ , the variance of  $\sigma^o(j)$ . The functional form for  $\xi^2(j)$  is given in Eq. (3). Note that in the measurement-based approach,  $\xi^2(j)$  can be chosen to be a function of either  $\sigma^o(j)$  or  $\sigma_c^o(j,\bar{\alpha})$ . Due to computational complexity, we choose to use the former.

As previously mentioned, the variables  $\sigma_{pix}^o(x,y)$  and  $\sigma^o(j)$  are related through the SeaWinds antenna point-spread function introduced in Eq. (2). The point-spread function acts as a mathematical operator that samples the two-dimensional space spanned by  $\sigma_{pix}^o(x,y)$  and produces backscatter values that lie in the backscatter space observed by

SeaWinds. Using Eq. (2), variables  $\sigma_c^o(x,y,\bar{\alpha})$  and  $\sigma_c^o(j,\bar{\alpha})$  also share this relationship. Consequently,  $\sigma_c^o(j,\bar{\alpha})$  can be interpreted as the backscatter value that results from projecting the  $j$ th SeaWinds antenna aperture onto the space spanned by the iceberg model.

Explicitly solving for the optimal measurement-based ML model estimates and including regularization terms to mitigate the adverse effects of extreme values of  $\xi^2(j)$  yields

$$\bar{\alpha}_{MB}^* = \underset{\bar{\alpha}}{\operatorname{argmin}} \sum_j \left[ \frac{(\sigma^o(j) - \sigma_c^o(j,\bar{\alpha}))^2}{\chi^2(j)} + \ln(\chi^2(j)) \right] \quad (12)$$

where  $\bar{\alpha}_{MB}^*$  is the parameter vector that minimizes the measurement-wise ML objective function and  $\chi^2(j) = (1 - \lambda_{MB}) + \lambda_{MB} \cdot \xi^2(j)$  where  $\lambda_{MB} \in [0, 1]$ . Similar to the image-based approach, the case where  $\lambda_{MB} = 0$  corresponds to a least-squares objective function and the case where  $\lambda_{MB} = 1$  corresponds to the unaltered measurement-based maximum-likelihood case. We can vary  $\lambda_{MB}$  to allow us to select an estimation approach that lies between these two cases which is helpful in mitigating the adverse effects of low variances. This is discussed further in Section 5.4.

Choosing  $\bar{\alpha}$  to maximize the objective function yields the best fit in the maximum-likelihood sense for the parameters of the model from the raw backscatter measurements. Repeating this for a time-series of raw measurement sets, we obtain the measurement-derived temporal evolution of the size and rotation of the iceberg. Note that in the noise-free case, both Eqs. (11) and (12) have a single maxima. However, in a noisy environment, neither Eq. (11) nor (12) is guaranteed to have a unique solution, therefore a search of the solution space is necessary.

#### 4.3. Algorithm comparison

Theoretical differences between the image-based and the measurement-based estimation methodologies are illustrated by expressing both approaches as optimization problems. The image-based estimation approach may be expressed as: minimize

$$\sum_{x,y \in X,Y} \left( \frac{\sigma_{pix}^o(x,y) - \sigma_c^o(x,y,\bar{\alpha})}{\chi_{pix}^2(x,y)} \right)^2 + \ln(\chi_{pix}^2(x,y)) \quad \text{[or equivalently maximize}$$

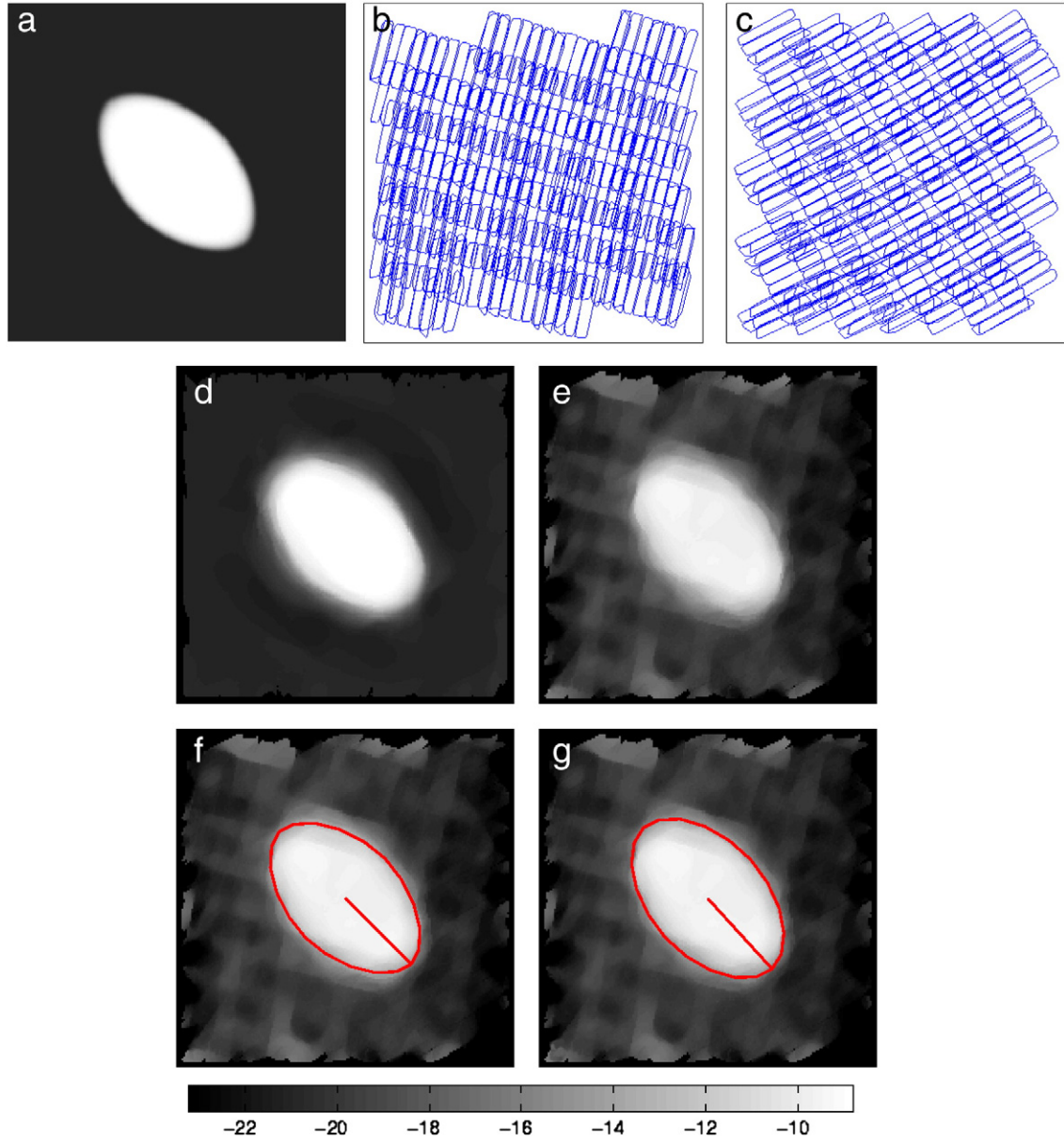


**Fig. 2.** Simulation results of estimating the size and orientation of an elliptical iceberg. a) The true iceberg model. b) A 6 dB-contour plot of the forward-looking SeaWinds slice measurements for a single pass. There are approximately 300 slices, each approximately 25 × 6 km in dimension. c) Aft-looking slice measurements for the same pass. d) SIR image created from noise-free backscatter values generated by projecting the antenna response functions from (b) and (c) onto the truth image (a). e) SIR image created from the noisy backscatter values. f) SIR image from (e) with an elliptical shape superimposed based upon image-based iceberg estimates. g) SIR image from (e) with an elliptical shape superimposed based upon measurement-based estimates. The colorbar is backscatter in dB. Images are approximately 125 × 125 km.

$P(\bar{\sigma}_{pix}^{\circ} | \bar{\sigma}_c^{\circ}(x, y, \bar{\alpha}))$  where  $\chi_{pix}^2(x, y) = (1 - \lambda_{IB}) + \lambda_{IB} \cdot \xi_{pix}^2(x, y)$  and  $\lambda_{IB} \in [0, 1]$ .

The measurement-based estimation approach may be expressed as: minimize  $\sum_j \frac{(\sigma_c^{\circ}(j) - \sigma_c^{\circ}(j, \bar{\alpha}))^2}{\chi^2(j)} + \ln(\chi^2(j))$  [or equivalently maximize

$P(\bar{\sigma}^{\circ} | \bar{\sigma}_c^{\circ}(j, \bar{\alpha}))$  subject to  $\bar{\sigma}_c^{\circ}(j, \bar{\alpha}) = A(\bar{\sigma}_c^{\circ}(x, y, \bar{\alpha}))$  where  $A(\cdot)$  is the linear sampling operator that maps the solution space spanned by the model to the observation space sampled by SeaWinds via the antenna impulse-response function and  $\chi^2(j) = (1 - \lambda_{MB}) + \lambda_{MB} \cdot \xi^2(j)$  where  $\lambda_{MB} \in [0, 1]$ .

The introduction of regularization terms enables us to trade off between information usage and problem conditioning. It changes the underlying problem so that the estimates are the projection of an underlying solution onto the spaces spanned by  $\bar{\sigma}_c^{\circ}(x, y, \bar{\alpha})$  and  $A(\bar{\sigma}_c^{\circ}(x, y, \bar{\alpha}))$ , respectively. Maximizing  $\lambda_{IB}$  and  $\lambda_{MB}$  ensures minimal projection error. Choosing  $\lambda_{IB}$  and  $\lambda_{MB}$  small mitigates the adverse effects of small variance terms, resulting in better-conditioned solution spaces. To illustrate the dependence of regularization on each estimation approach, multiple values of  $\lambda_{IB}$  and  $\lambda_{MB}$  are selected and compared in Section 5.

**Table 1**

Simulation results of the image-based and measurement-based ML estimates of the major axis, minor axis, and angle of orientation from Fig. 2. Both sets of estimates were calculated using the same noise realization.

	True value	Image-base estimates	Measurement-based estimates
$\rho_{ma}$ (km)	70.0	69.96	71.48
$\rho_{mi}$ (km)	42.0	41.98	43.22
$\theta$ (°)	45.0	45.0	47.6

**Table 2**

Statistics comparing the image-based and measurement-based ML estimation approaches in simulation with corresponding truth data. Statistics were created using 100 independent noise realizations.

Estimate Type	$\lambda$	$\rho_{ma}$ (km)		$\rho_{mi}$ (km)		$\theta$ (°)	
		Mean	STD	Mean	STD	Mean	STD
True	–	70.00	–	42.00	–	45.00	–
IB	0.00	69.96	0.029	41.98	0.021	45.00	0.011
IB	0.50	69.98	0.022	42.00	0.015	45.00	0.011
IB	0.75	70.00	0.025	42.00	0.017	45.00	0.016
IB	0.90	69.98	0.027	42.00	0.019	45.00	0.013
IB	0.99	70.00	0.022	42.00	0.013	45.00	0.013
IB	1.00	70.00	0.036	42.00	0.025	44.99	0.017
MB	0.00	70.12	0.40	42.16	0.35	45.11	1.05
MB	0.50	69.92	0.26	42.12	0.23	44.98	0.41
MB	0.75	70.02	0.27	42.24	0.26	45.07	0.55
MB	0.90	70.00	0.26	42.04	0.22	45.03	0.51
MB	0.99	69.92	0.26	42.10	0.40	45.11	0.49
MB	1.00	71.28	0.88	44.76	1.8	46.19	2.93

Both estimation approaches are constrained by the model. Since in practice, large tabular icebergs tend to have elliptical-like shapes, we generally obtain good results. The fact that the model does not precisely describe the actual iceberg shape is not critical for determining the

relative orientation and rotation angle which are of interest to scientists studying ocean currents that affect iceberg motion.

## 5. Performance

To explore the performance of both the image-based and model-based iceberg estimates, simulation is first employed. The utility of both approaches is then analyzed in a case study of iceberg A22a using actual data. Iceberg nomenclature is standardized by the United States National Ice Center (NIC) where the name begins with a letter corresponding to the quadrant where it was first detected, followed by an incremental number. As icebergs fragment, each fragment name is appended with a letter (NIC, update, 2010). Iceberg size and orientation estimates are analyzed using collocated high-resolution imagery and reports collected by the NIC. A time-series of extracted iceberg parameter estimates is also presented.

### 5.1. Simulation

Simulation is employed to analyze the effectiveness of both the image-wise and measurement-wise estimates. First, a synthetic truth image is generated using the iceberg model with  $\alpha$  parameters:  $A = -9$  dB,  $B = -21$  dB,  $n = 20$ ,  $p = 1.8$ ,  $\rho_{ma} = 35$  km,  $\rho_{mi} = 21$  km,

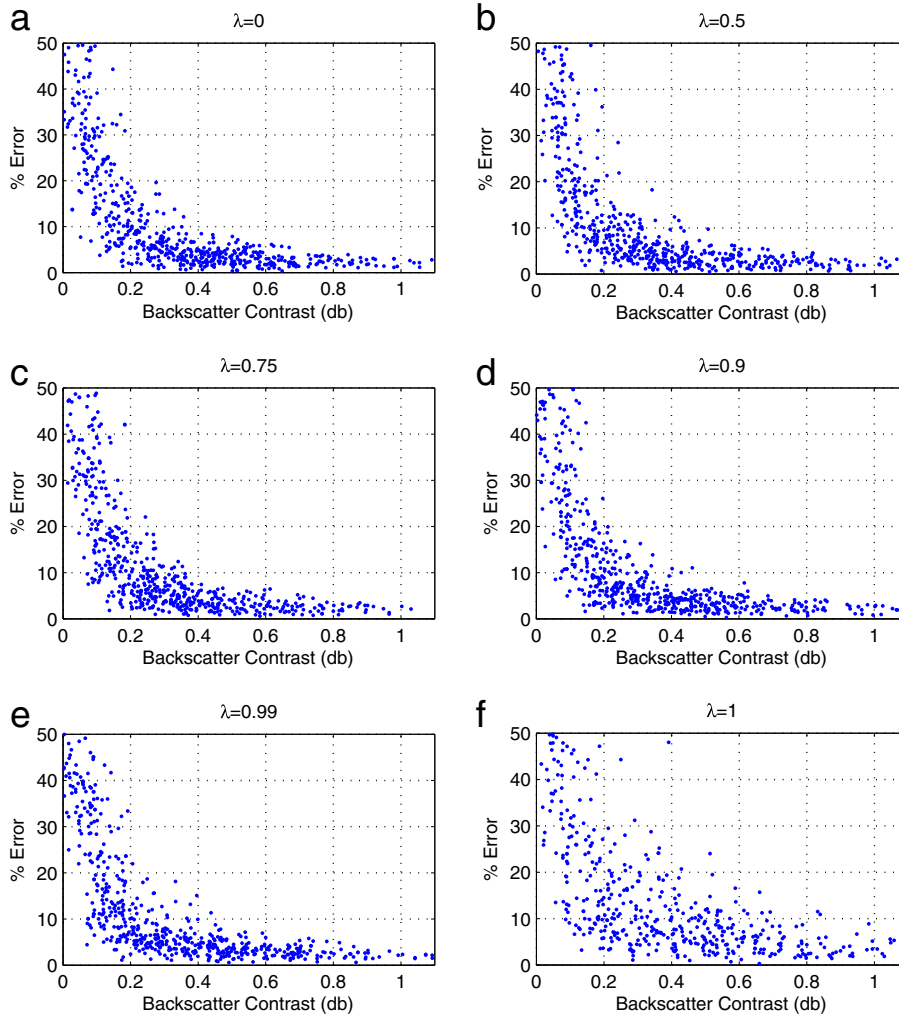


**Fig. 3.** Monte Carlo simulation results of the accuracy of IB iceberg parameter estimates with respect to the backscatter contrast between the iceberg and the surrounding medium for varying  $\lambda_{IB}$ . a–f) corresponds to  $\lambda_{IB} = [0.5 \ 0.75 \ 0.9 \ 0.99 \ 1]$ , respectively. The percent error metric is computed using the estimated major-axis length, minor-axis length, and angle of rotational orientation parameters according to Eq. (13).

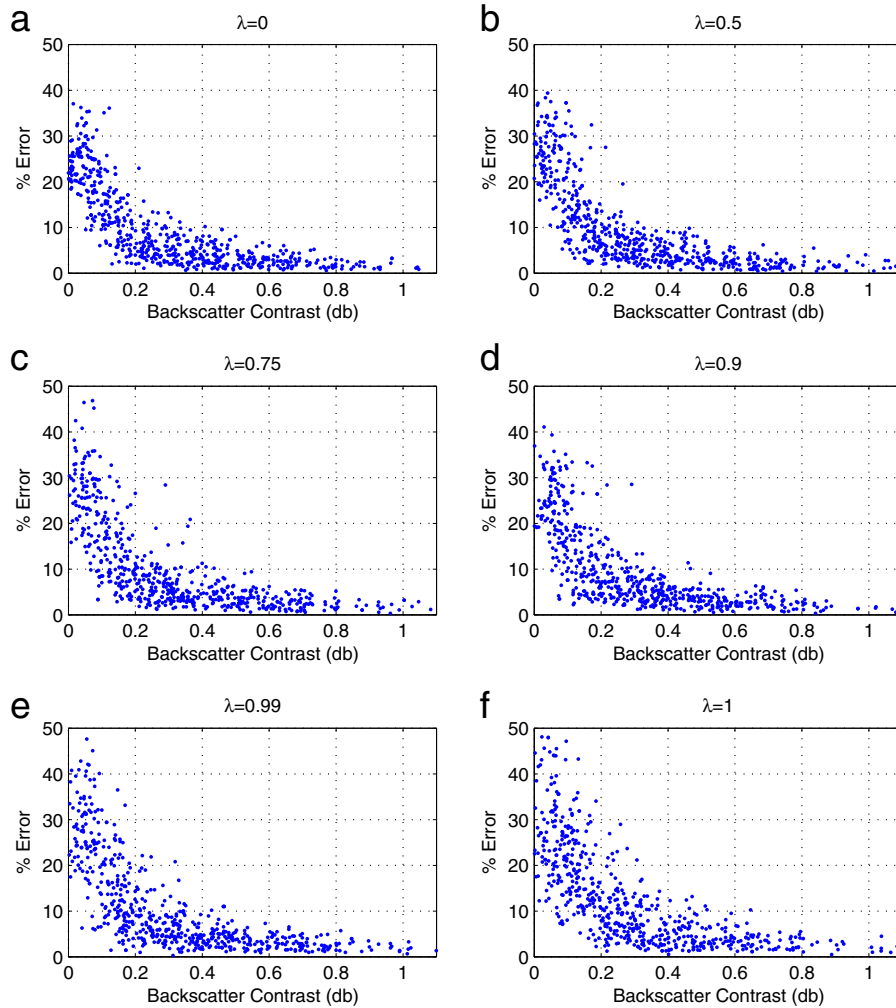


**Fig. 4.** Monte Carlo simulation results of the accuracy of MB iceberg parameter estimates with respect to the backscatter contrast between the iceberg and the surrounding medium for varying  $\lambda_{MB}$ . a–f) corresponds to  $\lambda_{MB} = [0 \ 0.5 \ 0.75 \ 0.9 \ 0.99 \ 1]$ , respectively. The percent error metric is computed using the estimated major-axis length, minor-axis length, and angle of rotational orientation parameters according to Eq. (13).

and  $\theta = 45^\circ$ . Actual SeaWinds antenna responses are used in simulation. The  $\mu_x$  and  $\mu_y$  location parameters correspond to a latitude and longitude of  $60.1888^\circ\text{S}$  and  $51.3135^\circ\text{W}$  on Julian day (JD) 100 of 2006.

The truth image is sampled by projecting the SeaWinds antenna response patterns from two passes of the SeaWinds sensor onto the truth image, generating simulated truth backscatter values  $\sigma_t^\circ$ . Observational boundaries are chosen to include two SeaWinds passes where each pass contains one forward look and one aft look, resulting in four total looks. Each look corresponds to approximately 300 slice measurements, resulting in a total of approximately 1200 backscatter measurements. To generate noisy  $\sigma^\circ$  measurements, Monte Carlo noise is added to the  $\sigma_t^\circ$  measurements using Eq. (3) where the  $\alpha$ ,  $\beta$ , and  $\gamma$  parameters correspond to the expected values for each observation.

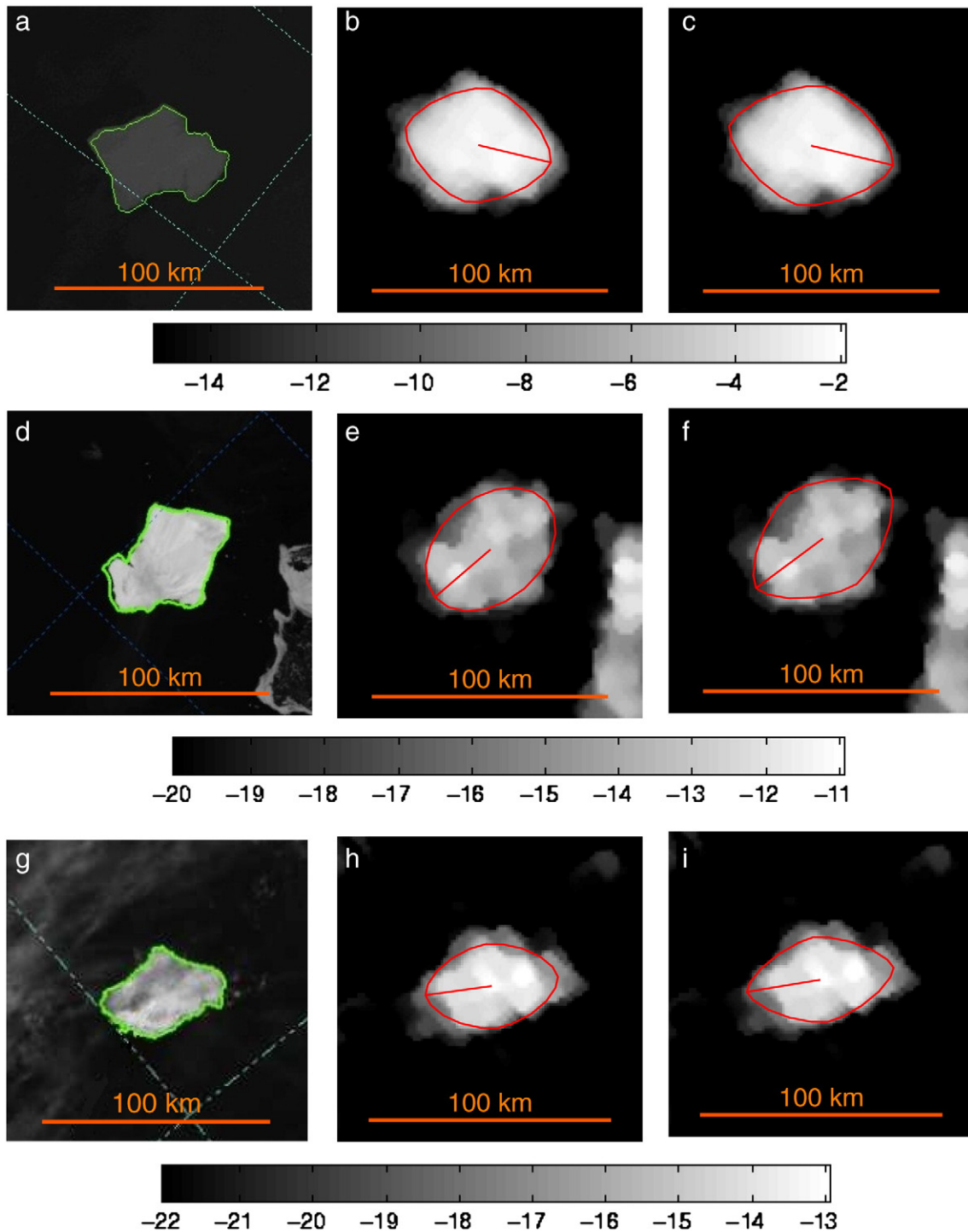
For the image-based estimation approach, the noisy  $\sigma^\circ$  values are processed into a corresponding SIR image and this backscatter image is used as the input into the image-based estimation process. For the measurement-based simulation, the noisy  $\sigma^\circ$  values are used directly in the estimation process.

Fig. 2a illustrates a simulated truth image where the iceberg is centered in the image. The 6 dB-contour of the forward and aft-looking slice aperture responses over the iceberg for a single pass is

displayed in Fig. 2b and c. The SIR image created from the truth dataset is displayed in Fig. 2d. The SIR image created from  $\bar{\sigma}^\circ$  is displayed in Fig. 2e, f, and g. Elliptical shapes based on iceberg size and orientation estimates are superimposed on Fig. 2f and g where the former corresponds to the image-based estimates and the latter to the measurement-based estimates. Values for both estimates are presented in Table 1. Note that both approaches perform relatively well, with the image-based estimates marginally closer to the true parameters.

To better analyze the utility of both estimation approaches, it is helpful to study the behavior of both methodologies given multiple noise realizations. The sensitivity of each approach is analyzed by sweeping  $\lambda_{IB}$  and  $\lambda_{MB}$ . One hundred simulations are performed for each estimation approach where  $\lambda_{IB} = \lambda_{MB} = [0, 0.5, 0.75, 0.9, 0.99, 1.00]$  and each has an independent noise realization. The resulting statistics are presented in Table 2. Note that the mean of both estimation approaches are close to the true values of  $\rho_{ma}$ ,  $\rho_{mi}$ , and  $\theta$ . While the mean of both algorithms are comparable, the standard deviation of the IB and MB estimates differ by an order of magnitude with the IB approach out-performing the MB algorithm.

From Table 2, the statistics for the simulated IB estimates show minimal variation with  $\lambda_B$ ; however, choosing  $\lambda_{IB} = 0.99$  maximizes information usage with minimal associated projection error. Similarly,



**Fig. 5.** Images and parameter estimates of iceberg A22a on days 2006 JD 110, 2006 JD 303, and 2007 JD 64. a) DMSR IR image for the first day. b) Elliptical shape based on image-based estimates superimposed on SeaWinds backscatter image for the first day. c) Elliptical shape based on measurement-based estimates superimposed on SeaWinds backscatter image for the first day. d) MODIS image for the second day. e) Elliptical shape based on image-based estimates superimposed on SeaWinds backscatter image for the second day. f) Elliptical shape based on measurement-based estimates superimposed on SeaWinds backscatter image for the second day. g) AVHRR image for the third day. h) Elliptical shape based on image-based estimates superimposed on SeaWinds backscatter image for the third day. i) Elliptical shape based on measurement-based estimates superimposed on SeaWinds backscatter image for the third day. Colorbars are backscatter in dB. Iceberg perimeter marking in the high-res. images was performed by the NIC. For estimate comparison, see Table 3.

choosing  $\lambda_{MB}=0.90$  provides an appropriate tradeoff by ensuring small overall variance while preserving maximum information usage.

In addition to observation noise, estimate accuracy is a function of backscatter contrast between the iceberg and surrounding medium. Simulation is used to quantify this relationship using the simulation parameters mentioned earlier. Estimation accuracy is quantified using a normalized error metric derived from the major-axis length,

minor-axis length, and angle of rotational orientation parameters such that

$$\% \text{ Error} = \frac{1}{3} \left( \left| \frac{\rho'_{ma} - 35 \text{ km}}{35 \text{ km}} \right| + \left| \frac{\rho'_{mi} - 21 \text{ km}}{21 \text{ km}} \right| + \left| \frac{\theta' - 45^\circ}{180^\circ} \right| \right) \cdot 100 \quad (13)$$

**Table 3**

Major axis, minor axis, and angle of orientation estimates of iceberg A22a using high-resolution (HR) imagery, estimates from SeaWinds data, and NIC reports. Angle of orientation is with respect to the image frame where horizontal is 0° and positive increasing is in the clockwise direction. For average error statistics with respect to values extracted from the high-res. images, see Table 4.

Estimates		2006 Julian day 110			2006 Julian day 303			2007 Julian day 64		
Type	$\lambda$	$\rho_{ma}$ (km)	$\rho_{mi}$ (km)	$\theta$ (°)	$\rho_{ma}$ (km)	$\rho_{mi}$ (km)	$\theta$ (°)	$\rho_{ma}$ (km)	$\rho_{mi}$ (km)	$\theta$ (°)
HR	–	61.7	45.2–53.7	14	62.4	39.9–47.3	142	51.3	29.7–34.9	167
NIC	–	67.7	50.0	–	67.7	50.0	–	44.5	37.0	–
IB	0.00	65.4	50.4	11	63.8	47.6	137	56.2	35.6	171
IB	0.50	64.5	49.9	13	62.0	43.7	139	55.2	35.1	172
IB	0.75	64.8	50.0	14	62.0	43.7	139	55.2	35.0	172
IB	0.90	63.7	49.8	13	62.0	43.7	139	55.2	35.0	172
IB	0.99	64.0	49.9	14	62.0	43.7	139	55.1	34.9	172
IB	1.00	63.9	49.8	13	62.0	43.7	139	55.2	35.0	172
MB	0.00	65.8	48.6	7	73.1	47.5	149	61.7	35.7	171
MB	0.50	66.8	48.5	8	70.7	47.6	143	61.3	35.4	171
MB	0.75	69.6	50.7	12	70.6	47.7	143	61.4	35.4	171
MB	0.90	72.2	52.2	13	70.4	47.8	143	61.4	35.3	171
MB	0.99	72.3	44.7	8	70.7	48.6	143	61.3	35.4	171
MB	1.00	50.6	22.3	11	79.3	62.3	136	72.4	36.1	172

where  $\rho'_{ma}$ ,  $\rho'_{mi}$ , and  $\theta'$  are the model parameter estimates. To deal with the 180° model direction ambiguity, Eq. (13) is calculated using the unwrapped  $\theta'$  about 180° to minimize the difference in the third term. The results are displayed in Figs. 3 and 4 for the IB and MB cases, respectively. The estimation error is inversely related to backscatter contrast. Note that the spread of estimates in both the IB and MB cases is consistent when  $\lambda_{IB}$  and  $\lambda_{MB}$  are less than unity, supporting the earlier observation that both estimation approaches benefit from regularization.

5.2. Case study

Both estimation techniques are applied to SeaWinds backscatter measurements of iceberg A22a. Iceberg A22a is selected because it is non-circular, it is visible for an extended period of time away from sea ice, and because collocated high-resolution optical imagery is available.

Three days are highlighted in this study: 2006 Julian days 110 and 303 and 2007 Julian day 64. For these days, annotated high-resolution images of iceberg A22a are available from DMSP, MODIS, and AVHRR and are displayed in Fig. 5a, d, and g. Corresponding SeaWinds backscatter images for the first day are displayed in Fig. 5b and c. Elliptical shapes based on iceberg size and orientation estimates are superimposed on the backscatter images where the image-based estimate ( $\lambda_{IB}=0.99$ ) corresponds to the former and the measurement-based estimate ( $\lambda_{MB}=0.90$ ) to the latter. Similarly, SIR backscatter images and corresponding elliptical shapes make up Fig. 5e and f for 2006 Julian day 303 and Fig. 5h and i for 2007 Julian day 64. Associated quantitative measurements are compared with NIC reports in Table 3.

In Table 3, note that for high-resolution images two values are extracted for the minor axis. The first minor axis estimate intersects the midpoint of the major axis at a 90° angle. The second is the largest possible value of the minor axis, without constraints. The SeaWinds image-based and measurement-based estimates fall between these two minor-axis lengths. Also, note the consistency of iceberg orientation between the high-resolution images and the SeaWinds estimates.

The average errors between the actual SeaWinds estimates and the values extracted from the high-resolution imagery are presented in Table 4. The average errors between parameters reported by the NIC and high-resolution data are also included in Table 4. Note that SeaWinds IB estimation errors show minimal variation with  $\lambda_{IB}$ , an observation consistent with simulation results. This behavior supports the selection of  $\lambda_{IB}=0.99$  in order to maximize information usage.

Also note the SeaWinds MB estimation errors are similar for  $\lambda_{MB} \leq 0.9$  with overall increasing errors for  $\lambda_{MB} > 0.9$ , demonstrating the need for regularization in the MB estimation methodology.

5.3. Time-series

Applying this estimation approach to a time-series of SeaWinds measurements, we obtain the temporal evolution of the iceberg's axis and rotation. Both the image-based and the measurement-based estimation algorithms are applied to SeaWinds measurements of iceberg A22a from 2006 Julian day 50 to 2007 Julian day 276. During this period, iceberg A22a is tracked in daily SIR images 553 out of 593 days in the MERS Antarctic Database (SCP, update, 2010). Image-based and measurement-based estimates are computed for each of the 553 days.

We can directly use the daily iceberg estimates computed using the IB and MB approaches, however to mitigate noise and measurement uncertainty, time-averaging estimates is helpful. A weighted time-average of the daily estimates over a short temporal window reduces the estimate variance and provides a more accurate estimate of iceberg parameters.

Estimates of the major axis of iceberg A22a are displayed in Fig. 6. SeaWinds IB and MB estimates are displayed in Fig. 6a and b, respectively. NIC estimates over the same interval are displayed in Fig. 6c. To highlight general trends, each dataset is filtered using a 71-pt

**Table 4**

Average errors of SeaWinds IB estimates, SeaWinds MB estimates, and NIC reports of the major-axis length, minor-axis length, and angle of rotational orientation with respect to high-resolution imagery of iceberg A22a on 2006 JD 110, 2006 JD 303, and 2007 JD 64. For underlying values, see Table 3.

Type	$\lambda$	$\rho_{ma}$ (%)	$\rho_{mi}$ (%)	$\theta$ (°)
		Avg error	Avg error	Avg difference
NIC	–	10	4	–
IB	0.00	6	1	4
IB	0.50	4	0	3
IB	0.75	4	0	3
IB	0.90	4	0	3
IB	0.99	4	0	3
IB	1.00	4	0	3
MB	0.00	15	1	6
MB	0.50	14	1	4
MB	0.75	15	1	2
MB	0.90	17	1	2
MB	0.99	17	7	4
MB	1.00	29	31	5

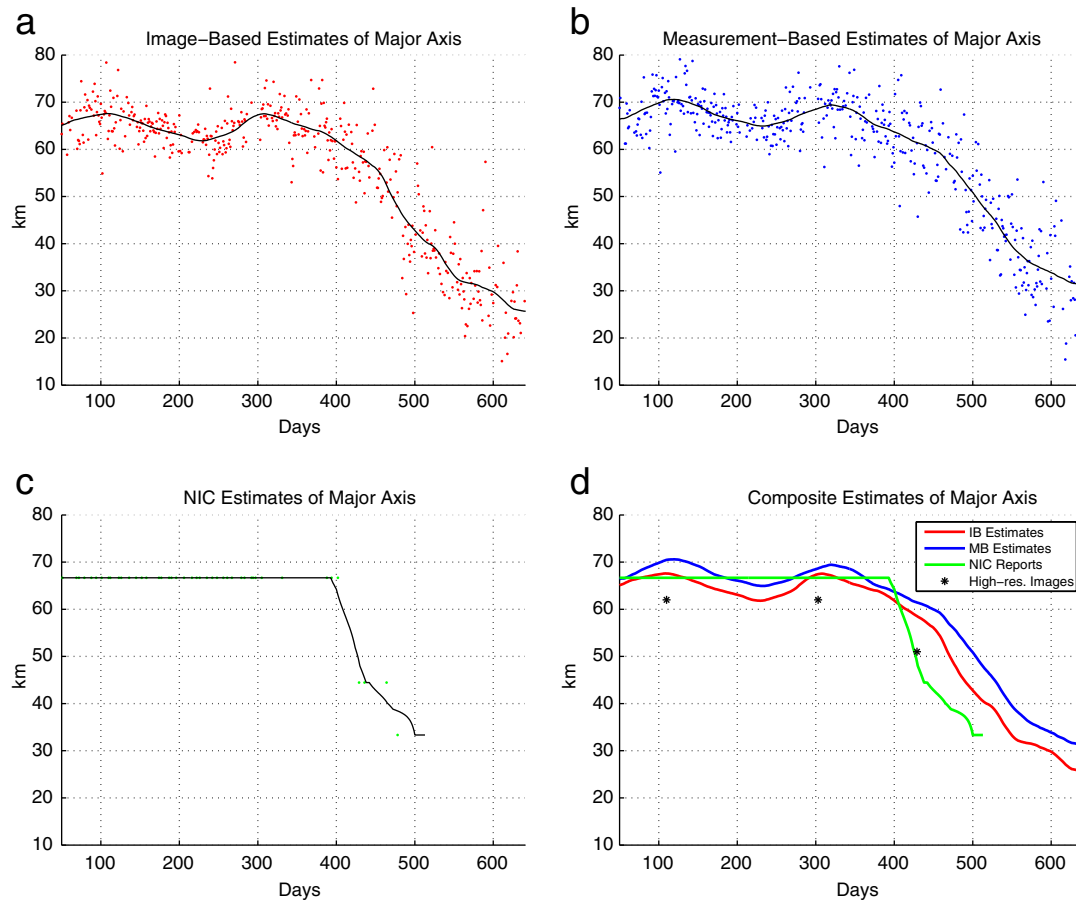


**Fig. 6.** Major axis comparisons of iceberg A22a from 2006 JD 50 to 2007 JD 276. JD 1 on the horizontal axis corresponds to 2006 JD 1. To highlight macro-scale trends, image-based estimates, measurement-based estimates, and NIC datasets were filtered using a 71-pt Epanechnikov filter and superimposed over the respective measurements. a) Image-based estimates of the major axis. b) Measurement-based estimates of the major axis. c) NIC estimates of the major axis. d) Composite trends of the major axis.

Epanechnikov filter, overlaid on each respective image. For comparison purposes, trend lines are displayed on Fig. 6d along with estimates derived from the high-resolution images from Section 5.2. Estimates of the minor axis are similarly displayed in Fig. 7. Note how the trends for both SeaWinds-based estimates reflect a gradual reduction in size as iceberg A22a moves away from the Antarctic continent, toward the warmer waters of the Antarctic Circumpolar Current. Dominant factors that contributed to the ablation of iceberg A22a are discussed in Section 5.4. For comparison, NIC axis trends have extended flat regions because the irregular reports are rounded to the nearest nautical mile. We note that NIC measurements vary in consistency because of changes in analysts (NIC, update, 2010).

Estimates of the local angle of rotation of iceberg A22a are displayed in Fig. 8a and b for image-based and measurement-based estimates, respectively. An 11-pt Epanechnikov filter is fitted to each set of  $\theta$  estimates to highlight net movement. Both trends are presented in Fig. 8c for comparison. Note that both sets of estimates are consistent in overall net movement.

Note that angle estimates are relatively consistent in shape until around day 450. This period in time corresponds to when iceberg A22a was moving rapidly from the Weddell Sea to the Scotia Sea along the iceberg corridor commonly called “Iceberg Alley”. Because icebergs are assumed to be spatially stationary during the estimation window (24 h), rapid movement during this period causes the iceberg profile to become smeared in daily SIR images, distorting iceberg estimates. One potential remedy for this situation is to shorten the estimation window, however the trade-off is a decrease in the number of measurements used in the minimization process and thus a reduced SNR in the estimation problem.

Statistics describing how many of the days have sufficient backscatter contrast to allow for accurate estimates are presented in Table 5. Conditions that result in inaccurate estimates during this period are discussed in the following section.

#### 5.4. Discussion

As previously mentioned, the image-based and measurement-based estimation algorithms successfully provide accurate estimates of iceberg A22a’s major-axis length, minor-axis length, and angle of rotational orientation for 421 (for  $\lambda_{IB}=0.99$ ) and 424 (for  $\lambda_{MB}=0.90$ ) days out of a total of 593 days, respectively. A discussion of why either or both of the estimation algorithms failed to produce valid estimates of iceberg parameters for the remaining days highlights the limitations of both estimation techniques.

Conditions that contribute to estimation inaccuracies may be divided into three categories: 1) contamination, 2) insufficient backscatter contrast, and 3) measurement sampling inconsistencies. Contamination can be further divided into a) cases where external high-backscatter targets are included in the frame of estimation, b) periods of iceberg fragmentation, and c) conditions where significant intra-day iceberg movement is present.

Inaccurate estimates resulting from having multiple high-scattering targets in the frame of estimation are expected and are stated in Section 2.3 as an assumption for the iceberg parameters estimation process. The probability of such an event occurring depends primarily upon external parameters, such as the presence of nearby glacial ice or sea ice. For example, an ambiguity may arise when sea ice has an associated backscatter as high as the backscatter from glacial ice (Stuart

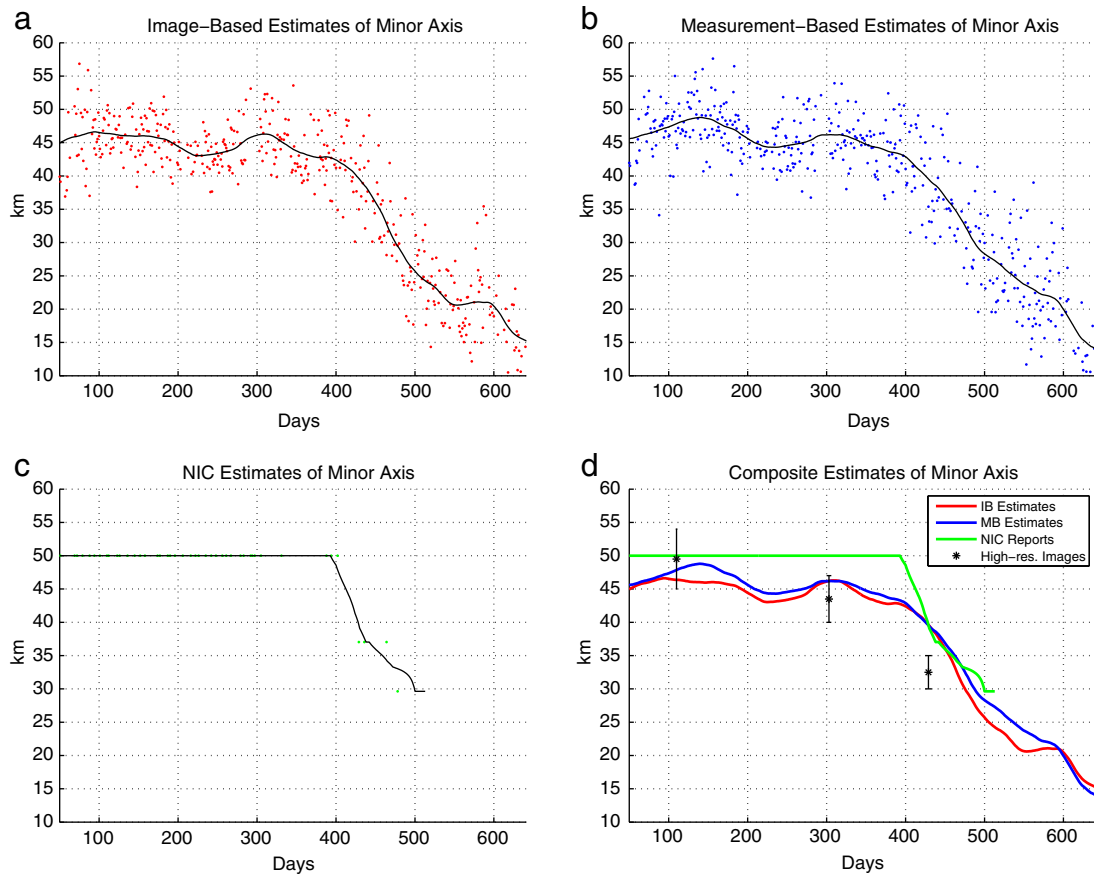


**Fig. 7.** Minor axis comparisons of iceberg A22a from 2006 JD 50 to 2007 JD 276. JD 1 on the horizontal axis corresponds to 2006 JD 1. To highlight macro-scale trends, image-based estimates, measurement-based estimates, and NIC datasets were filtered using a 71-pt Epanechnikov filter and superimposed over the respective measurements. a) Image-based estimates of the minor axis. b) Measurement-based estimates of the minor axis. c) NIC estimates of the minor axis. d) Composite trends of the minor axis.

and Long, 2011), such as the radar return from multi-year sea ice. The presence of sea ice may cause an ambiguity in the estimation process where the image-based or measurement-based models are inappropriately fitted to a combination of glacial ice and sea ice. Mitigation of this case of contamination is possible using the MERS Antarctic iceberg database to flag the proximity of nearby icebergs and using SeaWinds sea ice products to flag the presence of surrounding sea ice (SCP, update, 2010).

Contamination from multiple high scattering targets is also caused by iceberg fragmentation. Upon calving from the terminus of glaciers or ice sheets, large tabular icebergs experience varying degrees of ablative forces. These forces result in general perimeter melting and in some cases, large-scale iceberg fragmentation. After fragmentation, iceberg fragments commonly drift in close proximity, showing up as a single target in low resolution radar images, however, eventually the paths of the iceberg fragments diverge. For the case study of iceberg A22a, this is observed in only a few cases of the daily SeaWinds backscatter images. Note that while the reduction in size of iceberg A22a is caused by both perimeter melting and iceberg fragmentation, the low-resolution scatterometer data precludes us from being able to uniquely identify which method dominates in the ablative process (Kristensen, 1983; Scambos et al., 2005; Sergienko et al., 2004). As a result, an automated estimation algorithm must be applied with care.

The third cause of contamination is the violation of the assumption in Section 5.3 of negligible intra-day iceberg movement. For instance, if the SeaWinds measurements used to create the daily SIR backscatter image are recorded over an iceberg at the beginning and end of a day where significant iceberg movement is present, the reconstruction process may reconstruct a backscatter image where the single iceberg

appears as two icebergs that are spatially separated, resulting in an echo-like effect. This case of contamination is detectable using a priori knowledge of iceberg position, available in the MERS Antarctic iceberg database, in conjunction with temporal characteristics of SeaWinds measurements (SCP, update, 2010).

Factors that influence backscatter contrast and subsequent iceberg estimation include local environmental conditions and iceberg geometry. At Ku-band, environmental conditions that primarily affect scattering properties over the ocean include ablation, rain, and wind. Both ablation and rain influence surface moisture. The presence of surface moisture on an iceberg dampens the associated volume scatter, reducing the backscatter contrast between the iceberg and background. Similarly, rain roughens the ocean surface and high winds induce capillary waves on the ocean's surface which raise the overall backscatter from the ocean, lowering the image contrast ratio. Note that for both the image-based and measurement-based algorithms, these factors are observed as the dominant cause of inaccurate estimates produced in the iceberg A22a case study.

It is also important to note that as an iceberg is reduced in size due to ablation its associated backscatter signature decreases. Once an iceberg is reduced in size to the order of 5–6 km, the iceberg's backscatter intensity blends into ocean noise and remaining fragments are no longer detectable using SeaWinds measurements (Stuart and Long, 2011).

The third effect, which primarily affects MB estimates, is measurement sampling inconsistencies, specifically when a SeaWinds sampling swath passes over the iceberg location and only partially covers the frame of observation. This partial swath may bias the iceberg estimation, and while an estimate is produced, iceberg

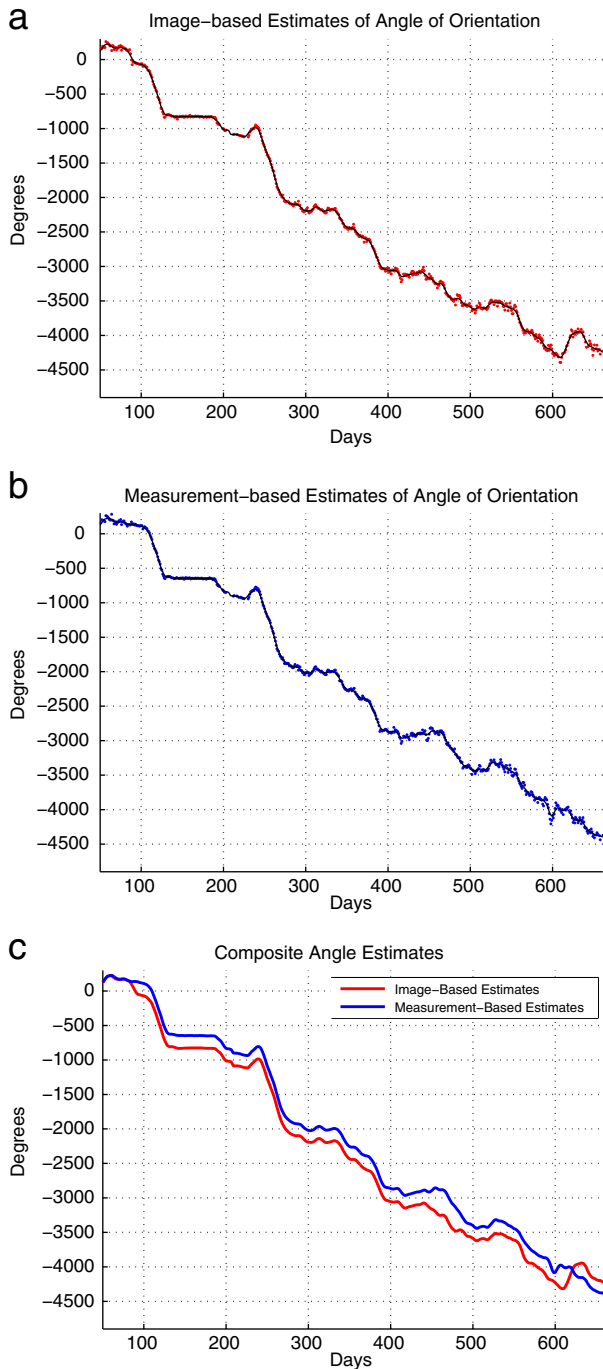


**Fig. 8.** Angle of rotational orientation estimates for iceberg A22a from 2006 JD 50 to 2007 JD 276. JD 1 on the horizontal axis corresponds to 2006 JD 1. A trend curve for each dataset is created using an 11-pt Epanechnikov filter to highlight net movement. a) Image-base estimates of  $\theta$ . b) Measurement-based estimates of  $\theta$ . c) Composite trend estimates of  $\theta$ . Rotation estimates have been unwrapped with respect to the initial day of study to show the rotational evolution of iceberg A22a. An increasingly positive angle corresponds to clockwise motion.

estimates are exaggerated with respect to the orientation of the antenna footprints. Note that if sufficient sampling exists over the whole frame of observation or if the partial sampling swath is captured within a sufficient temporal window, then the adverse effects of a partial swath are negligible. In the case study of iceberg A22a, estimate inconsistencies are observed when the temporal window becomes too large or if the total sampling density in the frame is sufficiently small such that the presence of a partial sampling

**Table 5**

Count and statistics of accurate daily SeaWinds IB and MB estimates of iceberg A22a from 2006 JD 50 to 2007 JD 276, a span of 593 days.

Type	$\lambda$	Estimate Count	$\rho_{ma}$ (km) STD	$\rho_{mi}$ (km) STD	$\theta$ ( $^\circ$ ) STD
NIC	–	44	1.7	0.7	–
IB	0.00	407	4.8	3.7	25.7
IB	0.50	437	5.0	3.7	25.4
IB	0.75	439	5.0	3.8	24.9
IB	0.90	437	5.0	3.9	24.7
IB	0.99	437	5.0	3.9	24.7
IB	1.00	421	5.1	3.9	25.3
MB	0.00	396	5.3	4.6	25.4
MB	0.50	426	5.1	4.3	25.2
MB	0.75	426	5.1	4.3	25.2
MB	0.90	426	5.1	4.3	25.0
MB	0.99	424	5.2	4.4	26.1
MB	1.00	84	4.8	2.9	30.0

swath is given enough weight to bias the cumulative measurements. The automatic detection of partial swaths in the observation frame is possible using the SIR image dataset (SCP, update, 2010).

## 6. Conclusion

In summary, we develop and evaluate two estimation algorithms to estimate an iceberg's major-axis length, minor-axis length, and angle of rotational orientation. The first algorithm is an image-based approach and the second is a measurement-based approach that uses raw SeaWinds measurements. Maximum-likelihood objective functions that relate backscatter to model-based simulated backscatter for each case are developed. Furthermore, each estimation approach is supplemented with regularization terms to mitigate the effects of small measurement variances.

The utility of both estimation approaches is analyzed in simulation where both approaches performed well on average. The performance of both approaches is found to improve with the inclusion of minimal regularization terms. On average, both estimation methodologies converge to true values; however, the standard deviation of the image-based estimates is improved by an order of magnitude over the measurement-based approach.

The utility of both estimation approaches is also analyzed in a case study of iceberg A22a where image-based estimates of the major and minor axes differ from true estimates extracted from high-resolution imagery to within an average of 2.3%. Measurement-based estimates differ by 12.2%, and NIC estimates differ by 7.2%. On average, SeaWinds image-based and measurement-based estimates of the angle of orientation differ from high-res. estimates by 3.2 $^\circ$  and 3.8 $^\circ$ , respectively. Coinciding with simulation results, image-based estimation is consistent regardless of regularization while measurement-based estimation is consistent for  $\lambda_{MB} < 1$ .

Next, a long-term analysis is performed using both approaches to estimate parameters of iceberg A22a from 2006 Julian day 50 to 2007 Julian day 276. During this span, 71% of the daily image-based estimates (for  $\lambda_{IB} = 0.99$ ) and 72% of the measurement-based estimates (for  $\lambda_{MB} = 0.90$ ) result in non-degenerate cases, compared with only 7% reported by the NIC over the same period. While both approaches are viable, the image-based iceberg size and orientation estimates out-perform measurement-based techniques and provide more accurate daily estimates of iceberg parameters from resolution-enhanced scatterometer images.

Even though SeaWinds was never designed to track icebergs, previous work has demonstrated the utility of using SeaWinds backscatter images to detect icebergs on a daily basis (Stuart and Long, 2011), and this study demonstrates the utility of using SeaWinds data to supplement iceberg position reports with estimates of size and

orientation. These estimates may be used to supplement other modeling processes related to iceberg and ocean current studies. Because the non-uniform shape of icebergs is important in iceberg dynamics models, the estimates proposed in this paper provide the necessary data to test model adequacy and potentially improve model predictions.

## References

- Ashcraft, I., Long, D., 2003. The spatial response function of SeaWinds backscatter measurements. *Proceedings of SPIE: Earth Observing Systems VIII*, Vol. 5151, pp. 609–618. Aug.
- Bigg, G., Wadley, M., Stevens, D., Johnson, J., 1997. Modelling the dynamics and thermodynamics of icebergs. *Cold Regions Science and Technology* 26 (2), 113–135 Oct.
- Crocker, G., 1993. Size distributions of bergy bits and growlers calved from deteriorating icebergs. *Cold Regions Science and Technology* 22 (1), 113–119 Nov.
- Dunbar, S., Weiss, B., Stiles, B., Huddleston, J., Callahan, P., Shirliffe, G., Perry, K., Hsu, C., QuikSCAT Science Data Product User's Manual. Version 3.0. JPL [ftp://podaac.jpl.nasa.gov/ocean\\_wind/quikscat/L2B/doc/QSUG\\_v3.pdf](ftp://podaac.jpl.nasa.gov/ocean_wind/quikscat/L2B/doc/QSUG_v3.pdf).
- Early, D., Long, D., 2001. Image reconstruction and enhanced resolution imaging from irregular samples. *IEEE Transactions on Geoscience and Remote Sensing* 39 (2), 291–302.
- Kristensen, M., 1983. Iceberg calving and deterioration in Antarctica. *Progress in Physical Geography* 7, 313–328.
- Long, D., Ballantyne, T., 2002. Is the number of icebergs around Antarctica increasing. *EOS, Transactions American Geophysical Union* 42, 469–474.
- NIC, 2010. National Ice Center. <http://www.natice.noaa.gov/>. 2010 update.
- Savage, S., Crocker, G., Sayed, M., Carrieres, T., 2000. Size distributions of small ice pieces calved from icebergs. *Cold Regions Science and Technology* 31 (2), 163–172.
- Scambos, T., Sergienko, O., Sargent, A., MacAyeal, D., Fastook, J., 2005. ICESat profiles of tabular iceberg margins and iceberg breakup at low latitudes. *Geophysical Research Letters* 32.
- SCP, Scatterometer Climate Record Pathfinder <http://www.scp.byu.edu/>. 2010 update.
- Sergienko, O., Scambos, T., MacAyeal, D., Fastook, J., 2004. Tabular icebergs in the Southern Atlantic: melt pond geometry, and margin evolution. *EOS, Transactions American Geophysical Union* 85 (47) C22A–07.
- Spencer, M., Long, D., 2000. Improved resolution backscatter measurements with the SeaWinds pencil-beam scatterometer. *IEEE Transactions on Geoscience and Remote Sensing* 38 (1), 89–104.
- Spencer, M., Wu, C., Long, D., 1997. Tradeoffs in the design of a spaceborne scanning pencil beam scatterometer: application to SeaWinds. *IEEE Transactions on Geoscience and Remote Sensing* 35 (1), 115–126.
- Stephen, H., Long, D., 2000. Study of iceberg B10A using scatterometer data. *Proceedings of the International Geoscience and Remote Sensing Symposium, Honolulu, HI*, Vol. 3, pp. 1340–1342.
- Stuart, K., Long, D., 2011. Tracking large tabular icebergs using the SeaWinds Ku-band microwave scatterometer. *Deep-Sea Research II* 58, 1285–1300.
- Troglio, G., Benediktsson, J., Moser, G., Serpico, S., 2010. Crater detection based on marked point processes. *Proceedings of the International Geoscience and Remote Sensing Symposium, Honolulu, HI*, pp. 1378–1381.
- Williams, B., Owens, M., Long, D., 2009. The ultra high resolution QuikSCAT product. *Proceedings of the IEEE Radar Conference, Pasadena, CA*, pp. 1–6.